On the Physics of Unstable Infiltration, Seepage, and Gravity Drainage in Partially Saturated Tuffs

B. Faybishenko[1], G. S. Bodvarsson, and R. Salve

Lawrence Berkeley National Laboratory, Earth Sciences Division

1 Cyclotron Road, MS 90-1116, Berkeley, CA 94720, USA

Abstract. To improve understanding of the physics of dynamic instabilities in unsaturated flow processes within the Paintbrush nonwelded unit (PTn) and the middle nonlithophysal portion of the Topopah Spring welded tuff unit (TSw) of Yucca Mountain, we analyzed data from a series of infiltration tests carried out at two sites (Alcove 4 and Alcove 6) in the Exploratory Studies Facility, using analytical and empirical functions. The analysis of infiltration rates measured at both sites showed three temporal scales of infiltration rate: (1) a *macro-scale* trend of overall decreasing flow, (2) a *meso-scale* trend of fast and slow motion exhibiting three-stage variations of the flow rate (decreasing, increasing, and [again] decreasing flow rate, as observed in soils in the presence of entrapped air), and (3) *micro-scale* (high frequency) fluctuations. Infiltration tests in the nonwelded unit at Alcove 4 indicate that this unit may effectively dampen episodic fast infiltration events; however, well-known Kostyakov, Horton, and Philip equations do not satisfactorily describe the observed trends of the infiltration rate. Instead, a Weibull distribution model can most accurately describe experimentally determined time trends of the infiltration rate. Infiltration tests in highly permeable, fractured, welded tuff at Alcove 6 indicate that the infiltration rate exhibits pulsation, which may have been caused by multiple threshold effects and

[1] Corresponding author. E-mail: BAFaybishenko@lbl.gov, Tel: (510) 486-4852

water-air redistribution between fractures and matrix. The empirical relationships between the extrinsic seepage from fractures, matrix imbibition, and gravity drainage versus the infiltration rate, as well as scaling and self-similarity for the leading edge of the water front are the hallmark of the nonlinear dynamic processes in water flow under episodic infiltration through fractured tuff. Based on the analysis of experimental data, we propose a conceptual model of a dynamic fracture flow and fracture-matrix interaction in fractured tuff, incorporating the time dependent processes of water redistribution in the fracture-matrix system.

Key words: fractured rock, infiltration, seepage, gravity drainage, infiltration equation.

Introduction

One of the most challenging problems in fractured rock hydrogeology is how to interpret the results of field and laboratory infiltration experiments. Field, laboratory, and modeling studies of water flow in heterogeneous soils and rocks show that water does not always flow as a uniform front, but sometimes exhibits a complex three-dimensional, channelized preferential flow pattern with complex time and scale variations in flow rate, rock saturation, and water pressure (Glass et al., 1989; Nativ et al., 1995; Pruess et al., 1999; Su et al., 1999; Dahan et al., 1999; Faybishenko et al., 2000; Podgorney et al., 2000). Field and laboratory investigations have also revealed the phenomenon of intrafracture water dripping (Podgorney et al., 2000; Geller et al., 2001). These studies show that asperity contacts in a fracture can lead to multiple threshold barriers affecting spatial and temporal flow patterns. Phase transitions in the air-liquid system can create temporal variations in pressure even under constant-flow-rate boundary conditions (Persoff and Pruess, 1995). However, a variety of processes may affect flow through fractured media, including gravity, capillarity, surface tension, viscosity, entrapped air, and biological activity.

A number of publications have considered both mechanisms of water flow—advection and diffusion—as well as concepts of double-permeability and double-porosity, which were reviewed by Pruess et al. (1999). The development of models from first principles requires the determination of parameters characterizing fracture flow and fracture-matrix interaction, which in most cases is difficult, if not impossible, to measure directly (Faybishenko and Finsterle, 2001). Having recognized that the complex processes of flow and transport in partially saturated fractured rock are unlikely to be simulated using a single model, Pruess et al. (1999) proposed to

use multiple models that will provide "complementary" aspects of unsaturated fractured flow behavior. One of the common approaches to the analysis of unsaturated flow in fractures is to assume an analogy to flow in partially saturated porous media, using Darcy's law and Richards' equation to describe the unsaturated hydraulic parameters (Pruess and Tsang, 1990; Persoff and Pruess, 1995; Tokunaga and Wan, 1997).

The goal of this paper is to improve understanding of the dynamic instabilities in liquid flow processes in partially saturated tuffs, through analysis of a series of infiltration tests in the Paintbrush nonwelded unit (PTn) and the middle nonlithophysal portion of the Topopah Spring welded tuff unit (TSw) at Yucca Mountain, using analytical and empirical functions. These tests were carried out in 1998 at Alcove 4, within the PTn in the Exploratory Studies Facility (ESF) (Wang et al., 2000; Salve and Oldenburg, 2001; Salve et al., 2000a), and at Alcove 6 of the ESF, within the welded tuff of the middle nonlithophysal portion of the TSw (Wang et al., 2000; Salve et al., 2002b; Doughty et al., 2002). In this paper, we analyze the results of these experiments using analytical and empirical functions and discuss the main factors and processes causing dynamic instability in the processes of *infiltration* (occurring at the surface), *intrinsic-fracture seepage* (occurring in fractures), *extrinsic-fracture seepage* (occurring at the intersection of a fracture with a rock cavity or another fracture), *matrix imbibition*, and *gravity drainage* (occurring as seepage [under gravity] from the formation after the water supply is stopped).

2. Experience from Investigating Partially Saturated Soils and Fracture Replicas

Laboratory experiments on soil cores and fracture replicas as well as small-scale field infiltration experiments provide a general understanding of the expected factors and processes of flow in

fractured porous media under field conditions. In addition to the conventional terms *saturated* and *unsaturated* hydraulic conductivity, we would like to use the term *quasi-saturated hydraulic conductivity* to define the hydraulic property of media containing entrapped air below the water table or in perched water zones (Faybishenko, 1995). For the case of infiltration from the surface into initially unsaturated macroporous soil or fractured rock, the magnitude of temporal variations in quasi-saturated hydraulic conductivity may be as much as two hundred percent, caused by the effects of entrapped air and microbiological processes. Figure 1 summarizes the main factors affecting the three-stage temporal variations in the quasi-saturated hydraulic conductivity below the surface during ponded infiltration for both laboratory and field conditions (Faybishenko, 1995; 1999). During the initial period of infiltration from the surface (*Stage 1*), water flows rapidly into the largest pores and is imbibed by a dry matrix. As water imbibes into an initially unsaturated matrix, it pushes air out from the matrix into the largest pores, thus blocking the largest pores by entrapped air and reducing the quasi-saturated hydraulic conductivity. As time progresses (*Stage 2*), entrapped air is discharged as air dissolves in water (because of temperature and pressure gradients) and removed either downward by moving water or upward under buoyancy. At this time, the quasi-saturated hydraulic conductivity may increase by about one to two orders of magnitude in laboratory air-tight cores, up to a maximum value that is essentially the saturated hydraulic conductivity, K_s. Under field conditions, when the water pressure underneath the near-surface skin layer drops below the air entry pressure, atmospheric air from the sides may enter the soils that become unsaturated, causing the infiltration rate to decrease and prohibiting the full saturation of the formation and the determination of the saturated hydraulic conductivity (Faybishenko, 1984; Faybishenko, 1986). The hydraulic conductivity may significantly decrease later (*Stage 3*), as a result of biofilms

growing in the pore space and blocking conducting pores. Microbiological activity may decrease permeability by as much as three orders of magnitude (Rittman, 1993). Other factors, such as deformation of the porous space and soil skeleton, swelling of soil particles, solute concentration, and shrinkage, may also affect hydraulic properties of soils (Luthin, 1957).

After the drainage of either soils (Dzekunov et al., 1987) or fractured rock (Faybishenko et al., 2000; Podgorney et al., 2000), new infiltration tests usually repeat a general three-stage pattern of the infiltration rate; however, exact values of the flux or the quasi-saturated hydraulic conductivity are not repeatable. Several small-scale (40 × 80 cm) ponded infiltration tests (Podgorney et al., 2000) conducted in fractured basalt at the Hell's Half Acre (HHA) Lava Field of southeastern Idaho also showed that the water-dripping frequency from the fracture exposed in the rock cave (located 1 m below the surface) was affected by a combination of the intrinsic-fracture flow and the capillary-barrier effect at the exit of the fracture, both of which exhibited several types of deterministic chaos (Faybishenko, 2000).

3. Description of Infiltration Experiments in Nonwelded and Welded Tuffs

3.1. Alcove 4 Infiltration Tests in Nonwelded Tuff

The tests at Alcove 4 in the ESF considered here were conducted from October 21 through November 5, 1998, to characterize hydraulic properties of the PTn unit and determine if the PTn unit can dampen episodic infiltration events before reaching the Topopah Spring welded unit (TSw)—the potential repository horizon (Salve and Oldenburg, 2001; Salve et al., 2002a). Figure 2a schematically illustrates the vertical cross section of the Alcove 4 Test Bed, in which several horizontal boreholes were drilled for water release and monitoring. The test bed

contained the following subunits of the PTn: Pah Canyon layer, the Pah Canyon bedded tuff, an argillic layer, a fault, and a fracture trace. The mean air permeability (k) of the discretely faulted and fractured nonwelded tuff at Alcove 4 is approximately 10^{-13} m^2, with a standard deviation of 0.93 for $\log(k)$ and air permeability of the fault is about one order of magnitude higher (Wang et al., 2000; Salve and Oldenburg, 2001). A horizontal slot was excavated and instrumented below the test bed to detect and capture water at the lower end of the test bed. However, during the experiments considered here, no water seeped into the slot, indicating that all water was absorbed by the formation or redistributed laterally within the formation.

The infiltration experiments included seven releases of water in Borehole 12 in a packed off cavity of 0.3 m long and 7.5 cm in diameter that intersected the fault approximately 1.40 m from the wall (Figure 2a). At the beginning of each test, 1.37 liters of water (the volume of the borehole packed off cavity) was released for about 3 minutes to fill up the borehole opening. Once a constant-head boundary condition (2-4 cm) in the borehole was established, flow rates were measured every minute for the duration of each test. To monitor migration of water, adjacent boreholes were equipped with electrical resistivity probes (ERPs) and psychrometers (Salve et al., 2000). Each infiltration test lasted between 4 and 7 hours (the duration of the tests was limited by the time permitted to work in the Yucca Mountain tunnel during the day shift), injecting 20–43 liters into the formation for each test. Overall, 193 liters of water were injected over a period of two weeks. The time between tests lasted from one day to a week (Wang et al., 2000). In their analysis of Alcove 4 infiltration experiments, Salve and Oldenburg (2001) found variations in intake rate over different time scales, inappropriateness of the application of Philip's equation derived for one-dimensional flow in the analysis of Alcove 4 infiltration tests, similarity

of temporal evolution of individual test intake rates, role of both matrix and fault in flow experiments, decrease in matrix sorption in a wetted system, and the potential capability of the PTn to dampen episodic infiltration pulses. Further details of the tests and numerical data analysis can be found in Salve and Oldenburg (2001) and Salve et al. (2002a). This paper provides an independent analysis of Alcove 4 infiltration tests, using analytical and empirical functions.

3.2. Alcove 6

Alcove 6 is located at the Northern Ghost Dance Fault within the middle nonlithophysal portion of the Topopah Spring welded tuff (TSw) unit in the potential repository horizon. Figure 2b illustrates the layout of the test bed at Alcove 6. Air permeability tests (Cook, 2000) in Borehole A identified a high-permeability zone with k of approximately 6.7×10^{-12} m^2, and a low-permeability zone with k of 2.7×10^{-13} m^2. According to a fracture mapping of the Alcove 6 wall, welded tuff includes discrete, subvertical fractures and relatively few subhorizontal fractures (Salve et al., 2002b). A series of infiltration tests was performed to characterize both permeability zones. Water was released in the Borehole A opening (cylindrical cavity of 0.3-m in length and 7.5 cm in diameter). Migration was monitored using an array of psychrometers and ERPs in Boreholes C and D, separated by a distance of 0.7 m and located 0.7 m and 0.6 m below Borehole A, respectively. A horizontal slot was excavated 1.6 m below the injection opening of Borehole A, in which collection trays were installed to capture seepage.

Two series of infiltration tests were carried out at Alcove 6: (1) infiltration into the low-permeability zone with water injection under a constant water level through a section located

0.75 to 1.05 m from the collar of Borehole A, with two phases of infiltration (Phase 1 - Tests LPZ-1 and LPZ-2, and Phase 2 - Test LPZ-3) separated by a break of 5.25 days, and (2) infiltration into the high-permeability zone through a section located 2.3 to 2.6 m from the collar of Borehole A, including Tests HPZ-1 and HPZ-2 conducted under a constant water level, and tests HPZ-3 through HPZ-8 conducted under constant inflow rates (Table 1). In their analysis of Alcove 6 infiltration experiments, Doughty et al. (2002) analyzed the breakthrough time and the fraction of water captured by the slot at the end of each test, using a 1D analytical solution for gravity flow, as well as 3D numerical modeling with a quasi-explicit fracture-network. They found that a model including both a primary and a secondary fracture network and fracture-matrix interaction is needed to match the behavior observed in the field. Further details of the tests and numerical data analysis can be found in Salve at al. (2002b) and Doughty et al. (2002). This paper provides an independent analysis of Alcove 6 infiltration tests, using analytical and empirical functions.

4. Results and Analysis

4.1. Infiltration Tests in a Fault Zone at Alcove 4

4.1.1. Temporal Scales of Flow Rate Variations

General trend. Figure 3a demonstrates the temporal variations of the infiltration rate for seven infiltration tests at Alcove 4, including: (1) the *macro-scale* trend of overall decreasing flow, (2) the *meso-scale* trend of fast and slow motion exhibiting three-stage variations of the flow rate (similar to those discussed in Section 2 for soils and fractured basalt), and (3) the

micro-scale (high frequency) fluctuations. We begin with the interpretation of meso-scale variations in the infiltration rate.

Meso-scale temporal variations include an initial fast motion, as the flow rate first rapidly decreases, and a slow motion, as the flow rate mildly increases and/or decreases or remains virtually constant. Figure 3b presents an expanded plot of the three-stage variations of the infiltration rate during Test 2. We explain the initially high infiltration rate observed during the first stage by two types of processes: a rapid infiltration into the fault zone caused predominantly by gravity forces, and an accelerated imbibition into the relatively dry surrounding tuff matrix caused by capillary forces. To assess the applicability of existing infiltration equations for describing the decrease in infiltration rate, we attempted to fit experimental data using the well-known equations of Kostyakov (1932), Horton (1940), and Philip (1969). Kostyakov's equation (1932) can be given as a function of the instantaneous flow rate versus time:

$$q(t) = -nat^{-(n-1)} \qquad (1)$$

where q is the infiltration rate, t is time, and a and n are fitting parameters. The flow rate predicted from Kostyakov's equation approaches zero for a large time, but does not approach a constant value, as could be predicted from Horton and Philip's equations.

Horton's equation is given by

$$q_d = (q(t) - q_{min}) / (q_{max} - q_{min}) = exp(-\beta t) \qquad (2)$$

where q_d is the dimensionless flow rate, q_{min} is the minimal flow rate, q_{max} is the maximum flow rate, and β is the decay parameter. Although Horton's equation is assumed to be empirical in modern literature (e.g., Jury et al., 1991), we note that in the original paper by Horton (1940) this equation was derived assuming that the reduction of q could be from exhaustion processes, including surface and fracture sealing caused by in-washing, swelling of colloids, redistribution of particles, microbiological clogging, as well as by entrapped air.

Philip (1969) developed a time-series solution for the flow rate caused by absorption into a uniform soil with an initially uniform moisture content. For short times, this solution can be approximated by its first four terms

$$q(t) = 0.5S\,t^{-1/2} + A + Bt^{1/2} + Ct + \ldots \qquad (3)$$

in which parameter S is called sorptivity, and A, B, and C are coefficients. According to Philip, the two leading terms of Equation (3) represent the solution for one-dimensional flow, with the entire Equation (3) representing a two- or three-dimensional flow process. It may be assumed that the first term of Philip's equation describes fast infiltration into initially unsaturated media as affected by strong capillary forces developed at the beginning of infiltration. It is further assumed that as time goes on, the effect of capillary forces becomes negligible in comparison with gravity forces that are taken into account by the second term of Philip's equation. For many soils, the $t^{-1/2}$ dependence of the plunging part of the flow rate curve is limited to 3–10 minutes (Hillel, 1982).

As an example of comparing experimental data and fitting curves, Figure 4 presents the experimental data and those calculated from Kostyakov's, Horton's, and Philip's equations for Test 3. Coefficients summarized in Table 2 were evaluated based on solving nonlinear regressions using the Levenberg-Marquardt method (using software CurveExpert 1.3, Starkville, MS). Figure 4a shows that Kostyakov's equation slightly overpredicts the initial decrease in the flow rate, and its tail tends to decrease faster than was observed in the experiment. Figure 4b indicates that Horton's equation describes relatively well the initial decrease in the infiltration rate, but does not take into account that at later times the flow rate is still decreasing. Figures 4c shows that a two-term Philip's equation overpredicts the initial decrease in the flow rate and approaches the asymptotic value of $q_{\min}$ = 56.83 ml/min too quickly, which implies that flow is not one-dimensional even at the beginning of the test. Figures 4d and 4e indicate that the three- and four-term Philip's equations slightly improve the fit, but do not describe experimental data satisfactorily. Moreover, Table 2 indicates that the coefficients of Philip's equation vary with the number of equation terms, which implies that these coefficients are just fitting polynomial coefficients and are not medium parameters.

To develop an empirical model for analyzing experimental data, we employ the Weibull distribution function, which is often used in biology, engineering, agriculture, and economics to describe the failure rate of complex systems with a varying failure parameter, which changes monotonically and approaches a final value asymptotically. The use of this function is reasonable to assume that (1) the decrease in the infiltration rate is caused by a failure of water-conducting paths to transfer water, either because of blockage of these paths (macropores, fractures) or a

decrease in the hydraulic gradient; and (2) the asymptotic decrease in the flow rate is typical for multidimensional flow (Philip, 1969). The Weibull's distribution function for the infiltration rate versus time can be given by

$$q_d = (q(t) - q_{min})/(q_{max} - q_{min}) = 1 - \exp(-s\, t^d) \qquad (4)$$

with four parameters: q_{max} is the initial (maximum) flow rate, q_{min} is the minimum (asymptotic) flow rate, s is the scale factor, and d is the shape factor (note that a negative d is required to get a decrease in q with time). The advantage of this function is the scaling of the time variable, which permits us to simulate a flexible shape for the infiltration curve, and a better approximation of the gradual decrease in the flow rate to the asymptotic value of q_{min}. The Weibull model parameters are compared to other equation parameters in Table 2 for Test 3 at Alcove 4 and are compared for all seven tests in Table 3. Visual inspection of Figure 4 and statistical parameters (standard error and correlation coefficient) summarized in Table 2 indicate that the Weibull function describes the experimental data better than the other equations. (Only Test 5 showed slightly better approximation of experimental data using Horton's function.)

Infiltration tests indicate that the initially high flow rate decreases for the first 10–20 minutes of infiltration by a factor ranging from 1.25 to 2.4. The overall asymptotic flow rate decrease (q_{max}/q_{min}) ranges from 2.1 to 4.25, which indicates that the nonwelded unit investigated at Alcove 4 may effectively dampen initial fast infiltration events. Figure 4g shows that normalized (dimensionless) infiltration rates versus time calculated from Equation (4) are practically the same only for Tests 2 through 7 and are different from that for Test 1. This

comparison suggests that the same processes are being involved in water flow in each successive test after the first infiltration test. However, the overall decrease in the infiltration rate suggests the influence of an additional factor affecting the water migration on the macro-scale, as will be described below.

The maximum and minimum infiltration rates could be used to estimate tentatively the range of hydraulic conductivity of the composite fault-matrix tuff formation. We assume that for each test, the initially high infiltration rate (q_{max}) is mainly affected by flow through the fault, the minimum infiltration rate (q_{min}) is affected by flow through both the fault and the matrix, the hydraulic gradient is unity, and the flow area corresponds to the lower half of the cylindrical surface of the borehole opening. Using these assumptions, the permeability of the fault and the volume-averaged values characterizing fault-matrix media were calculated from Darcy's law and are summarized in Table 3. Estimated permeabilities for the fault range from 8.7×10^{-12} to 1.6×10^{-11} m^2, which are about 3 to 6 times less than the value of 5×10^{-11} used in 3D numerical modeling of the Alcove 4 infiltration tests (Salve and Oldenburg, 2001). The calculated permeability from infiltration tests could be underestimated for several reasons: q_{max} was measured a few minutes after the beginning of the test, and thus a real maximum value could have been missed; the actual cross-sectional area for flow through the fault could have been less than that of the borehole opening; entrapped air could have reduced the flow rate; or a quasi-saturated formation could have occupied only the zone in the near vicinity of the borehole injection interval, so that the saturated hydraulic conductivity of rocks would not have been reached, as is often the case with soils (see Section 2). The relatively high values of permeabilities calculated from q_{min}, predicted from the Weibull equation, confirm that both the

fault and the matrix were involved in the flow process, as found by Salve and Oldenburg (2001). We cannot determine analytically the contribution of flow through the fracture and the matrix without numerical modeling. Nevertheless, these results support the assumptions used by Ho (2001) in developing a semianalytical solution for one-dimensional infiltration in unsaturated fractured rock. Ho used the mass-conservation equation for an equivalent-continuum medium (Peters and Klavetter, 1988) and assumed an equilibrium between liquid in the fracture and rock matrix, so that no net exchange occurs between the two media.

The second stage of the temporal increase in flow rate can be explained by the increase of rock saturation as entrapped air is removed and water is imbibed into the matrix. This stage is clearly observed in Tests 1 and 2, and some slight increases occur in Tests 4 and 6. The decrease in the flow rate for the third stage is consistent with the overall macro-scale trend of the decrease in the flow rate, which is demonstrated in Figure 3a.

In general, the Alcove 4 data agree with those of Peters et al. (1987), who investigated water imbibition into a sample of a nonwelded tuff (PTn) and determined two distinct rates of imbibition - fast and slow. Peters et al. (1987) further determined that a 60% saturation develops during water imbibition into tuff. In describing the mechanisms of these changes, they employed a concept of air entrapment during the fast flow phase, followed by air redistribution within the porous space, which is consistent with the hypothesis we employ in this study to explain the initial decrease in the flow rate.

Macro-scale temporal trend represents the overall decrease in the flow rate from test to test. Because Test 1 is likely to involve flow processes different from those at later times (see Figure 4g), we fitted the trend of infiltration rates for Tests 2 through 7, considering only the periods of slow motion for each test. Table 4 shows that all equations tested produce a relatively good fit with experimental data. However, Philip's equation generates a negative parameter *A,* which is not physically reasonable. We suggest that the observed macro-scale decrease in the infiltration rate is associated with the increase in the rock saturation after each test, leading to a decrease in flow rate due to reduced imbibition potential (Philip, 1969), and factors and processes causing a final decrease in the flow rate for the 3rd stage of infiltration tests (as described in Section 2).

Micro-scale temporal variations could have been caused by slight fluctuations of the water level in the water supply system and current fluctuations generated by the data acquisition systems. They are not considered in this paper for Alcove 4.

4.1.2. Travel Time along a Fault

Water injected in Borehole 12 was detected in Borehole 11 by electrical resistivity probes located between 0.65 and 2.40 m from the collar. Based on the geometry of intersection of Boreholes 12 and 11 with the fault (see Figure 2a), arrival time is inferred to represent travel time to the fault. Figure 5 presents at Borehole 11, as a function of the mean infiltration rate. The mean infiltration rate for each test was calculated as

$$q_{mean} = \frac{1}{T_{ar}} \int_0^{T_{ar}} q dt$$

with the limits of integration between 0 and the arrival time, T_{ar}, for each test. These data show that for a one-day break between infiltration tests (solid lines), the arrival time for the next test decreases, because less water is imbibed by the matrix. As the time between tests increases to 4 days (between Tests 2 and 3) and 7 days (between Tests 5 and 6), shown by dashed lines in Figure 5, the arrival time for the next test increases, which indicates that during a break between infiltration events in excess of 1 day, the fault desaturates, so that imbibition into the matrix during next test delays the arrival at Borehole 11. A comparison of the water arrival times for Tests 1 and 5 shows that despite a decrease of the mean infiltration rate from 137 to 72 ml/min, the arrival time decreased from 220 min to 104 min, indicating a higher apparent water velocity through the fault, presumably due to a decrease in water absorption by the matrix. Three-dimensional numerical simulations would be needed to capture actual water velocities (e.g., Salve and Oldenburg, 2001).

4.2. Infiltration Tests in the Fracture-Matrix Test Bed at Alcove 6

4.2.1. Infiltration Tests at the Low-Permeability Zone

Figure 6a shows that both Phases 1 and 2 exhibited the same exponential decline in the infiltration rate despite an interruption in the water supply for 5.25 days between phases. Because the infiltration rate observed at the end of Phase 1 matches very well that at the beginning of Phase 2, Figure 6a shows a break of 0.1 day (selected arbitrarily) instead of 5.25 days. The decrease in the infiltration rate, q, with time, t, can be described by the Horton equation (2) with

the following fitting parameters: q_{min} = 0.01 ml/min (fixed in this calculation), q_{max} = 12.635 ml/min, and β =2.28 min^{-1} (R=0.999). It is important to emphasize that the infiltration rate decreased smoothly, unlike the pulsing phenomena observed at the high-permeability zone (see Section 4.2.2 below). The initially high value of the first point on Figure 6a, which is not described by Horton's equation, was supposedly caused by the fast initial water accumulation in the borehole injection interval or fast water imbibition in the near-borehole zone. The departure of the last two points in Figure 6a from the exponential function (2) indicates the end of infiltration rate decrease, as was observed in experiments with soils, undergoing a transition from Stage 1 to Stage 2 (see Figure 1, Section 2).

The same trend and values of the infiltration rates before and after the 5.25-day break indicate that capillary forces tightly held water in pores, not allowing water to drain under gravity, not allowing atmospheric air to enter the system between the tests. Using the same assumptions in calculations of permeability as those used in analysis of the Alcove 4 infiltration tests, as described in Section 4.1.1, we calculate that the permeability of the low-permeability zone at Alcove 6 ranges from 4.7×10^{-16} to 6×10^{-13} m^2 (Table 5). For comparison, permeability that was used in numerical modeling to match field observations during the LPZ test was 5×10^{-15} m^2 (Doughty et al., 2002). We conclude from the results of this test that welded tuff in Borehole A at Alcove 6 is a relatively low permeability medium, with no large fractures exposed within the borehole injection interval.

4.2.2. Infiltration Tests in the High-Permeability Zone

4.2.2.1 Time Variation of the Infiltration Rate

Alcove 6 infiltration tests in the high-permeability zone demonstrated macro-, meso-, and micro-scale temporal variations of the infiltration rate *different* from those observed at Alcove 4. We will begin again with the meso-scale variations. Figure 6b shows the time variation of the infiltration rate measured during two constant head infiltration tests - HPZ-1 and HPZ-2. For the first 15 minutes (early part of Period 1 indicated in Figure 6b) of Test HPZ-1, the flow rate was low. However, the first measurement, taken 5 minutes into the test, could have failed to detect the initial high flow rate. During Period 2, the overall exponential increase in the flow rate can be described by an exponential equation

$$q(t) = q_{max} - (q_{max} - q_{min}) \exp(-\beta t) \quad (5)$$

with parameters summarized in Table 5.

During a 4.5-hour break in the water supply, air may have entered the rock, because the HPZ-2 test commenced with a lower infiltration rate (Period 3 in Figure 6b). The flow rate recovered sharply to a maximum value at 180 min as mobile air was removed from the flow channel, presumably by infiltrating water. The process of removing entrapped air from fractured tuff was much faster than that observed in soils (5 to 10 days and more according to observations in soil cores by Dzekunov et al., 1987). After the flow rate returned to the maximum value, it

decreased again with time according to the exponential Horton formula (4) with fitting coefficients summarized in Table 5. Period 3 ended with an abrupt decrease in the flow rate, which could have been caused by blockage of the fracture pathways by entrapped air. The recovery of the infiltration rate was very quick, followed again by the Hortonian decrease in the flow rate (Period 4).

Macro-scale variations. The variations of the infiltration rate during periods of slow motion (tail of the infiltration rate curve for Periods 2, 3, and 4) can characterize macro-scale variations of the flow rate. Numbers in bold in Table 5 show the overall decrease in the infiltration rate from 130 to 90 ml/min, which consistent with the decrease in the estimated permeability of the high-permeability zone at Alcove 6 from 6×10^{-12} to 4.3×10^{-12} m^2. (Calculations were performed using the same approach as that for the Alcove 4 and LPZ-1 of Alcove 6 infiltration tests.) The estimated values of permeability are well within the range determined from air-injection tests given by Wang et al. (2000) and correspond to the value of 6.8×10^{-12} m^2 that was used in modeling to match field observations (Doughty et al., 2002).

Micro-scale variations. To characterize the type of micro-scale instability in the infiltration rate, we plotted Figure 6c, which is the phase-plane diagram of the infiltration rate given as the relationship between dq/dt and q. This figure illustrates two groups of points for the unstable infiltration rate: (1) slow motion points within an oval representing unstable flow rate fluctuations (with small dq/dt) , and (2) fast motion along the curves (drawn schematically) in Figure 6c. Such attractors, which are common in describing nonlinear physical processes, are typical for pulsations and relaxation oscillations (Rabinovich et al., 2000).

4.2.2.2. Seepage Rate

For the infiltration tests discussed in the previous section, the relationship between the cumulative seepage measured at outlet trays and the cumulative infiltration volume for different infiltration rates is shown in Figure 7a. Based on these data, we can identify four stages in the temporal evolution of the seepage behavior, shown in Figure 7a, using Test 6 as an example:

Stage I. No seepage while water was initially injected into the rock. At this time, water was imbibed by the matrix and accumulated in fractures above the fracture exit (at the slot ceiling) that served as a temporary capillary barrier.

Stage II. Rapid discharge of water accumulated in the fracture, as a percolation threshold of the capillary barrier is exceeded.

Stage III. Gradual transition to a quasi-steady state, and

Stage IV. Quasi-steady state regime of infiltration and seepage rates (note that a steady-state regime may not develop or in some cases no seepage is recovered, though injection continues).

The seepage rate exceeds the infiltration rate in a few instances, as a result of temporal and local spatial instabilities in seepage. Figure 7b illustrates the relationship between the quasi-steady state seepage (calculated as the average value of the quasi-steady state portion of a seepage rate curve, Stage IV, shown by open squares for each test in Figure 7b) and the infiltration rate can be approximated by a linear function

$$Seepage = 0.822\ Infiltration - 4.488 \quad (6)$$

shown by the dashed black line in Figure 7b. In Equation (6), the seepage and the infiltration rates are in milliliters per minute. Figure 7b shows that the gap between the black dashed line (from Equation 6) and the one-to-one black solid line (indicating the conditions that the seepage and infiltration rates are equal) increases with increasing infiltration rate, suggesting more flow diversion as infiltration increases. Assuming in Equation (6) a seepage rate of zero (i.e., the extrapolation of the dashed black line to the infiltration rate axis), we can calculate the infiltration threshold of 5.46 ml/min for seepage to occur (note that term "infiltration threshold for the seepage to occur" that we use here is sometimes called "seepage threshold" [Finsterle and Trautz, 2001; Trautz and Wang, 2001]). This number is consistent with the result of Test 4 carried out under the infiltration rate of 5 ml/hr, which did not generate gravity drainage, because all water was supposedly retained in the fracture and the matrix or diverted around the slot or evaporated. For longer infiltration tests, as imbibition into the saturated matrix decreases, the seepage rate is expected to increase, implying a departure from Equation 6 with time. However, the seepage rate is not likely to approach the infiltration rate because a certain portion of water may be diverted around the slot due to the capillary barrier effect.

To illustrate the instability of the flow behavior, Figure 7c depicts the bifurcation tree structure of the seepage phase-plane, indicating that the magnitude of fluctuations (ds/dt) increases and is comparable with the seepage rate, s (the function itself). However, the seepage phase-plane is quite different from that for infiltration (Figure 6c), indicating that different processes are involved in infiltration and seepage. In interpreting the results of the investigation

of the seepage rate, note that the slot excavated in the unsaturated fractured rock is supposed to disturb (to a certain degree) the natural process of water migration in the subsurface. First, the ceiling of the slot may serve as an artificial capillary barrier, above which water may accumulate until the formation above the slot becomes saturated, so that a positive pressure develops. Alternatively, if a negative pressure is applied in the slot, it will create a driving force to overcome the capillary barrier effect and enhance downward flow. A collection tray is supposed to gather only water seeping under positive pressure (above atmospheric pressure), while water under a negative capillary pressure will remain in the formation, but can be diverted around the ceiling of the slot. Second, the tunnel ventilation may cause evaporation of seeping water from the slot ceiling, which is currently investigated using small-scale seepage tests at Yucca Mountain (Trautz and Wang, 2001). This evaporation may create a stronger hydraulic gradient at the lower boundary, but it also may cause the underestimation of the seepage rate. The cumulative effect of these processes requires further investigations.

4.2.2.3. Imbibition

Imbibition here is defined as a process of water absorption by the matrix and lateral flow and is determined to be the difference in the volume of water supplied into the subsurface and collected in the slot. Figure 7d shows that the imbibition (at the end of each test) was higher during Phase 1 of the tests (Tests 1-4) and decreased in Phase 2 (Tests 5-8), and that the imbibition depends on the infiltration rate. The solid line shows a power-law fit for the relationship between the imbibition and the infiltration rate for the first phase. The dependence of imbibition on the infiltration rate implies that different flow paths within a fracture network were likely involved as the infiltration rate increased.

4.2.2.4. Water Travel Time

To determine the arrival time of the leading edge of the water front, we used the time of the appearance of the first water drop in the collection tray in the slot at Alcove 6. Figure 8 shows the water travel time to the collection tray as a function of the infiltration rate. The relationship between the water travel time (T) and the infiltration rate (q) for Tests 3 through 8 can be approximated by a power-law function given by

$$T = \alpha q^{\gamma} \tag{7}$$

where α and γ are coefficients. (The departure of points for Tests 1 and 2 in Figure 8 from the trend for the rests of the tests indicates higher initial matrix imbibition.) Figure 8 shows no apparent hysteresis for the water travel time as the infiltration rate increases or decreases for Tests 3 through 8. Power-law Equation (7) indicates the scaling in the water travel time, which, in turn, implies the self-similarity in the geometry of the leading edge of the water front, which is common for many physical problems (Barenblatt, 1996). Equation (7) obtained from experimental data also agrees with a power law Kostyakov infiltration Equation (1). Comparison of Equations (1) and (8) gives $\alpha = 1/(an)$ and $\gamma=1/(n-1)$.

4.2.2.5. Gravity Drainage

Gravity drainage is defined as the volume of water that seeps under gravity from the formation into the collection tray after the water supply is stopped. The volume of gravity

drainage characterizes the water capacity in excess of the water held in the formation under capillary forces or diverted around the opening. Figure 9a shows the cumulative gravity-drainage versus time for different tests. Test 2 (98 ml/min) shows that gravity drainage occurs as a pulsation phenomenon, which may have been generated by multiple intrafracture threshold effects caused by fracture asperities and capillary barrier effects. However, Test 3 (53 ml/min) did not indicate pulsation. Other tests do not contain enough measurements to conclusively identify the presence of a pulsing effect.

Figure 9b shows that the relationships between the cumulative gravity drainage (calculated as per cent of the volume of water remaining in the formation at the end of the infiltration test) and the infiltration rate are different for Phase 1 (August 4-6) and Phase 2 (August 25-26) of the infiltration experiments. From Figure 9b, the gravity drainage is 16–19% of the total volume of water remaining in the rock, indicating a strong capillary suction in the formation. The smaller gravity drainage during Phase 1 compared to Phase 2 confirms a larger matrix imbibition (or larger water retention) during Phase 1, as was determined from the analysis of seepage phenomena. The calculated infiltration threshold at which gravity drainage occurs is approximately 5 ml/min (see Figure 9b). This value is consistent with the result of Test 4, with the infiltration rate of 5 ml/min, which produced no gravity drainage. The physical meaning of the infiltration threshold for gravity drainage is the same as that for the infiltration threshold for seepage to occur, and both values are approximately the same, 5 ml/min. The dependence of gravity drainage on the infiltration rate implies the need to simulate flow in fractured media using flow-rate dependent water-retention curves and models simulating non-equilibrium effects in the formation (Barenblatt et al., 2002).

5. Discussion and Conclusions

Infiltration processes in both the fracture and matrix components of fractured rock interact in a complex and highly variable fashion. At Alcove 4, the *macro-scale* temporal trend of overall flow-rate decrease is independent of the *meso-scale* temporal variations, occurring for the duration of each test. The meso-scale variations include a fast-motion period of decreasing flow rate and a slow-motion period of mild increasing and decreasing, or practically constant flow rate. We can infer that a decrease in the flow rate to the values observed at the end of the slow motion of the previous test indicates that hydraulic conductivity (which is the saturation-dependent parameter) is re-established after the passage of the fast pulse for each test. The same type of initial decrease in the flow rate at the beginning of each test indicates that during each break, the fault zone was partially drained, causing free air to enter the fault.

According to the conventional soil-science approach, under ponding infiltration in partially saturated media, the pressure gradient affecting the flow rate depends on both the height of ponding water and the capillary pressure at the wetting front. However, in fractured rock, the wetting front progresses not only downward, but also backward into the matrix, leading to a decrease in the pressure gradient and (accordingly) the infiltration rate. Comparing the flow behavior observed in a series of infiltration tests at Alcove 4 (see Figure 2) with that observed in porous media (see Figure 1) leads us to assume that entrapped air is one of the main factors affecting hydraulic conductivity of tuffs. Moreover, that a conventional two-term Philip's equation does not describe experimental data suggests that a one-dimensional Richards equation with monotonic hydraulic parameters is inadequate for infiltration tests in fractured formation,

because of gravity-driven flow with fingering effects in fractures (Eliassi and Glass 2001) and redistribution effects between fractures and matrix.

The presence of fast and slow types of flow for each infiltration test allows us to infer that flow behavior can be described by a dual-continuum model of double-porosity or double-permeability media, with flow-rate dependent functions for unsaturated hydraulic conductivity and water retention. Dynamic effects of fracture-matrix interaction under infiltration can be introduced into the dual-continuum model of flow using a time-dependent (or flow-rate dependent) moisture content, which will characterize the redistribution of water between the fracture and the matrix. For example, the water pressure Φ can be expressed as a function of both the moisture content Θ and its time derivative of $\mathrm{d}\Theta/\mathrm{d}t$

$$\Phi = f(\Theta, \mathrm{d}\Theta/\mathrm{d}t)$$

The application of this concept will lead to *Hallaire's model* (Hallaire, 1961) for flow in partially saturated media, which was developed for structured soils, and the application of which for water flow and evaporation was discussed by Rode (1965) and Feldman (1988).

At the highly permeable zone of Alcove 6, the infiltration rate's strong temporal oscillations around its general trend suggest the spontaneous water redistribution between different fractures. In welded tuff, when the infiltration rate increases, more fractures are likely involved in flow, intensifying the processes of extrinsic seepage, imbibition, and gravity drainage. As a result, both seepage and imbibition rates are proportional to the infiltration rate,

implying the dynamic effect of the system behavior. Figure 10 illustrates a concept of dynamic fracture flow pattern and fracture-matrix imbibition in fractured rock, including (1) flow-through fractures, (2) dead-end fractures, (3) fractures connecting flow-through fractures, and (4) matrix. This concept implies that the increase in the infiltration rate involves flow in additional connecting and dead-end fractures, which also enlarges the area of the fracture-matrix interaction and increases the matrix imbibition. Figure 10 also illustrates that the water pressure Φ, which is measured in a certain volume of the formation, depends on the flow regime, i.e., it varies for different flow rates q_1, q_2, and q_3, and can be expressed as a function of both the moisture content Θ and its time derivative $d\Theta/dt$. This conceptual model is consistent with the active fracture model of Liu et al. (1998), who hypothesized that only a saturation-dependent portion of connected fractures are active in conducting water.

It is important to emphasize a possibility of the coexistence of both negative and positive water pressures on the local scale in unsaturated fractured rock. The presence of extrinsic seepage indicates that water was under positive pressure in the fracture, and the presence of imbibition indicates that water was under negative pressure in the matrix. The dynamics of extrinsic seepage and gravity drainage depend on several factors, such as multiple threshold effects caused by fracture asperities within the fracture, matrix imbibition, and the capillary barrier effect above the slot. Dynamic effects of intrinsic seepage in fractures are the cause for the different types of attractors for the infiltration and extrinsic seepage rate. The travel time of the leading edge of the wetting front is described by a power law equation (7), which implies scaling and self-similarity phenomena for the water front geometry. In other words, the

distribution of the water front at any time can be obtained from that at a different time by a simple transformation given by a power-law equation.

The hallmark of nonlinear dynamic processes in water flow through welded tuff are high-frequency fluctuations of the infiltration and seepage rates (in our specific case determined for infiltration tests within the middle nonlithophysal portion of the Topopah Spring welded tuff), a nonlinear relationship between the gravity drainage and the infiltration rate, as well as scaling and self-similarity determined for the relationship between the water travel time and the infiltration rate. The knowledge that microscale fluctuations are chaotic is important, because such behavior is likely to generate chaotic and fractal properties of chemical diffusion processes in fractured tuff and will affect the description of diffusion-reaction systems. The simulation of infiltration tests requires the development of a model that takes into account the dynamic effects of flow in a multiple-fracture system. Because field-monitoring methods cannot accurately establish physical processes of intrafracture flow from direct observations, it is important to look for phenomenological models to describe the flow behavior (Pruess et al., 1999).

Acknowledgment

Discussions and review by Stefan Finsterle, Curt Oldenburg, Christine Doughty, and Robert Trautz, discussions with Karsten Pruess and Joe Wang, as well as useful critique by David Rogers and an anonymous reviewer are very much appreciated. The comments by Daniel Hawkes improved the readability of the paper. This work was supported by the Director, Office of Civilian Radioactive Waste Management, U.S. Department of Energy, through Memorandum Purchase Order EA9013MC5X between Bechtel SAIC Company, LLC, and the Ernest Orlando

Lawrence Berkeley National Laboratory (Berkeley Lab). The support is provided to Berkeley Lab through the U.S. Department of Energy Contract No. DE-AC03-76SF00098.

References

Barenblatt, G. I., Scaling, self-similarity, and intermediate asymptotics, New York: Cambridge University Press, 1996.

Barenblatt, G. I., T.W. Patzek, and D.B. Silin, The Mathematical Model of Non-Equilibrium Effects in Water-Oil Displacement, SPE 75169, 2002.

Cook, P., In situ pneumatic testing at Yucca Mountain, Int. J. Rock Mech. Min. Sci., 37, 357-367, 2000.

Dahan, O; Nativ, R; Adar, EM; Berkowitz, B; Ronen, Z. Field observation of flow in a fracture intersecting unsaturated chalk, *Water Resear. Res. 35*(11), 3315-3326, 1999.

Doughty, C., R. Salve, and J.S.Y. Wang, Liquid release tests in unsaturated fractured welded tuffs: II. Numerical Modeling. *Journal of Hydrology*, 256, 80-105, 2002.

Doughty, C., R. Salve, and J.S.Y. Wang, Liquid release tests in unsaturated fractured welded tuffs: II. Numerical Modeling. *Journal of Hydrology*, 256, 80-105, 2002.

Dzekunov, N.E., I.E. Zhernov, and B.A. Faybishenko, *Thermodynamic methods of investigating the water regime in the vadose zone*, Moscow, Nedra, 177 p., 1987.

Eliassi, M. and R. J. Glass, On the continuum-scale modeling of gravity-driven fingers in unsaturated porous media: The inadequacy of the Richards equation with standard monotonic constitutive relations and hysteretic equations of state, *Water Resour. Res*., 37(8), 2019-2035, 2001.

Faybishenko, B., Chaotic Dynamics in Flow Through Unsaturated Fractured Media, Report LBNL-46958, Lawrence Berkeley National Laboratory, Berkeley, California, 2000.

Faybishenko, B., and Finsterle, S., Tensiometry in fractured rocks, *In* Zhang, D., and Winter, C.L., eds., Theory, Modeling, and Field Investigation in Hydrogeology: A Special Volume in Honor of Shlomo P. Neuman's 60th Birthday: Boulder, Colorado, Geological Society of America Special Paper 348, p. 161–174, 2000.

Faybishenko, B., C. Doughty, M. Steiger, J. Long, T. Wood, J. Jacobsen, J. Lore, and P. Zawislanski, Conceptual model of the geometry and physics of water flow in a fractured basalt vadose zone, *Water Resour. Res.*, 37(12), 3499-3522, 2000.

Faybishenko, B., Comparison of laboratory and field methods for determination of unsaturated hydraulic conductivity of soils, In Proceedings of the International Workshop *Characterization and Measurement of the Hydraulic Properties of Unsaturated Porous Media*, van M. Th. Genuchten et al. (ed.), 279-292, 1999.

Faybishenko, B., Hydraulic behavior of quasi-saturated soils in the presence of entrapped air: laboratory experiments, *Water Resour. Res.*, 31(10), 2421-2435, 1995.

Faybishenko, B.A, Water-Salt Regime of Soils Under Irrigation: Agropromizdat, Moscow, 314 p., 1986.

Feldman, G. M., Water Movement in Thawing and Feezing Soils, Novosibirsk, "Nauka," Sibirskoe otd-nie, 1988.

Finsterle, S. and R.C. Trautz, Numerical modeling of seepage into underground openings, Mining Engineering, pp. 52-56, September 2001.

Geller, J.T., S. Borglin, and B. Faybishenko, Water seepage in unsaturated fractures: Experiments of dripping water in fracture models and chaos analysis, Report LBNL-48394, Lawrence Berkeley National Laboratory, Berkeley, California, 2001.

Glass, R.J., J.-Y. Parlange, and T.S. Steenhuis, Wetting front instability: 2. Experimental determination of relationship between system parameters and two-dimentional unstable flow field behavior in initially dry porous media: *Water Resour. Res*., 25, 1195-1207, 1989.

Hallaire, M., Irrigation et utilisation reserves naturelles: Ann. Agr., v.12, no.1, 1961.

Hillel, D. Introduction to soil physics, Daniel Hillel. New York : Academic Press, 1982.

Ho, C.K., A semianalytical solution for steady infiltration in unsaturated fractured rock, Water Resour. Res. 37(8), 2285-2289, 2001.

Horton, R.E., An approach toward a physical interpretation of infiltration-capacity. *Soil Sci. Soc. Am. Proc.*, 5, 399-417, 1940.

Jury, W.A., W.R. Gardner, and W.H. Gardner. Soil Physics, New York, J. Wiley, 1991.

Kostiakov, A. N., On the dynamics of the coefficient of water percolation in soils and on the necessity for studying it from a dynamic point of view for purposes of amelioration. In: Trans., 6th Comm. Int. Soc. Soil Sci., Russian Part A: 17-21, 1932.

Liu, H. H., C. Doughty, G. S. Bodvarsson, An active fracture model for unsaturated flow and transport in fractured rocks, Water Resour. Res., 34(10), 2633-2646, 1998.

Luthin, J.N. (Ed.), *Drainage of Agricultural Lands.* Am. Soc. Agron., Madison, Wisconsin, 1957.

Nativ, R., E. Adar, O. Dahan, and M. Geyh, Water recharge and solute transport through the vadose zone of fractured chalk under desert conditions: Water Resour. Res., 31(2) 253-261, 1995.

Persoff, P. and K. Pruess. Two-phase flow visualization and relative permeability measurement in natural rough-walled rock fractures, *Water Resour. Res.*, *31*(5), 1175-1186, 1995.

Peters, R. R., and E. A. Klavetter, A continuum model for water movement in an unsaturated, fractured rock mass, *Water Resour.Res*., *24*, 416–430, 1988.

Peters, R.R., E.A. Klavetter and J.T. George, Measuring and modeling water imbibition into tuff, In: D.D. Evans and T.J. Nicholson, Flow and Transport through Unsaturated Fractured Rocks, Geophysical Monograph 42, AGU, Washington D.C., 1987.

Philip J.R., Theory of infiltration, Adv. Hydrosci. 5:215-296, 1969.

Podgorney, R., T. Wood, B. Faybishenko, and T. Stoops, Spatial and temporal instabilities in water flow through variably saturated fractured basalt on a one-meter scale, AGU Geophysical Monograph 122 "Dynamics of Fluids in Fractured Rock," 129-146, 2000.

Pruess, K. and Y. W. Tsang, On two-phase relative permeability and capillary pressure of rough-walled rock fractures, *Water Resour. Res., 26*(9), 1915-1926, 1990.

Pruess, K., B. Faybishenko, and G. S. Bodvarsson, Alternative concepts and approaches for modeling flow and transport in thick unsaturated zones of fractured rocks, *Journal of Contaminant Hydrology - Special Issue*, 38, 281-322, 1999.

Rabinovich, M.I., A.B. Ezersky, and P.D. Weidman, The Dynamics of Patterns, World Scientific, 2000.

Rittman, B.E., The significance of biofilms in porous media, *Water Resour. Res., 29*(7)*,* 2195-2202, 1993.

Rode, A.A. *Background of the Theory of Soil Moisture*, Vol. 1, Gidrometeoizdat, Leningrad, 663 p., 1965.

Salve, R., C.M. Oldenburg, and J. S. Wang, Fault-matrix interactions in nonwelded tuff of the Paintbrush Group at Yucca Mountain, This Issue, 2002a.

Salve, R., J.S.Y. Wang and C. Doughty, Liquid release tests in unsaturated fractured welded tuffs: I. Field investigations. *Journal of Hydrology*, 256: 60-79, 2002b.

Salve, R., and C. M. Oldenburg, Water flow in a fault in altered nonwelded tuff. *Water Resources Research,* 37: 3043-3056, 2001.

Salve, R., J.S.Y. Wang and T.K. Tokunaga, A probe for measuring wetting front migration in rocks. *Water Resources Research,* 36: 1359-1367, 2000.

Su, G.W., J.T. Geller, K. Pruess, and F. Wen, Experimental studies of water seepage and intermittent flow in unsaturated, rough-walled fractures: *Water Resour. Res., 35*(4), 1019-1037, 1999.

Tokunaga, T.K., and J. Wan, Water film flow along fracture surfaces of porous rock, *Water Resour. Res. 33*(6), 1287-1295, 1997.

Trautz, R.C. and J.S.Y. Wang, Evaluation of seepage into an underground opening using small-scale field experiments, Yucca Mountain, Nevada, Mining Engneering, pp. 41-44, December 2001.

Wang, J.S., P.J. Cook, R.C. Trautz, Q.Hu, abd R.Salve, In situ field testing of processes, ANL-NBS-HS-000005, Rev. 00, 2000.

LIST OF FIGURES

Figure 1. Schematic of three-stage variations of the flow rate (q) and quasi-saturated hydraulic conductivity (K) with time under ponded infiltration in laboratory and field conditions. Lower portion of figure shows individual processes that increase (+ sign) or decrease (– sign) q and K (Faybishenko, 1995; Faybishenko, 1999).

Figure 2. Vertical cross sections of the layout of injection and monitoring wells: (a) Alcove 4, and (b) Alcove 6, in the ESF at Yucca Mountain (Wang et al., 2000).

Figure 3. (a) Infiltration rate vs. cumulative time for seven infiltration tests (numerals on the plot) in Alcove 4. A black line is the fit of the macro-scale temporal trend for slow motion periods of Tests 2 through 7, using the Weibull equation with parameters summarized in Table 4, and (b) Expanded view of the infiltration rate vs. time for Test 2, illustrating the meso-scale three-stage behavior. Experimental data are 5-point averaged.

Figure 4. Infiltration rate measurements and fitted curves for Test 3: (a) Kostyakov equation, (b) Horton equation; (c) Philip's equation with two terms, (d) Philip's equation with three terms, (e) Philip's equation with four terms, (f) Weibull distribution function, and (g) normalized Weibull functions for seven infiltration tests.

Figure 5. Water travel time at the fault as measured in Borehole 11. Numerals are test numbers.

Figure 6. (a) Infiltration rate vs. time for Alcove 6, LPZ-1, showing no difference in the flow rate decline despite a 5.25 day break in water supply between; thick line is an exponential fit using Horton's equation (2), (b) Infiltration rate vs. time for constant-head tests HPZ-1 and HPZ-2, with a 4.25 hr break in water supply between tests; thick lines are curves from Equations (2) and (5), and (c) Phase-plane diagram in coordinates dq/dt vs. q, and a schematic of the attractor that is typical for relaxation oscillations. Experimental data are 5-minute averaged values.

Figure 7. (a) Cumulative seepage (% of injected water) vs. the cumulative injected water for Alcove 6 tests; four stages (I through IV) of the seepage behavior are illustrated for Test 6, (b) Seepage rate vs. infiltration rate; black dashed line is a linear fit to the relationship between the quasi-steady state seepage (shown by open squares for each test) vs. the infiltration rate), (c) Phase-plane of seepage rate in coordinates ds/dt vs. s (numbers in the legend are infiltration rates), (d) Total imbibition and lateral flow (at the end of each test) vs. the infiltration rate. Digits are test numbers.

Figure 8. Travel time of the leading edge of the water front to the ceiling of the slot vs. the infiltration rate. For Tests 1 and 2, horizontal lines are the range of the flow rate.

Figure 9. (a) Cumulative gravity drainage vs. time for different flow rates (the data are from Wang et al., 2000; Salve et al., 2002b), (b) Gravity drainage (% of remaining water) vs. infiltration rate showing different trends for Phases 1 and 2. Digits are test numbers.

Figure 10. Illustration of a concept of a dynamic fracture flow pattern and fracture-matrix interaction. 1. Flow-through fractures, 2. Connecting fractures, 3. Dead-end fractures, 4. Matrix. Figure also illustrates that the water pressure $\Phi=f(\Theta,d\Theta/dt)$, which is measured in a certain volume of the formation (shown by a circle), may depend on the flow regime.

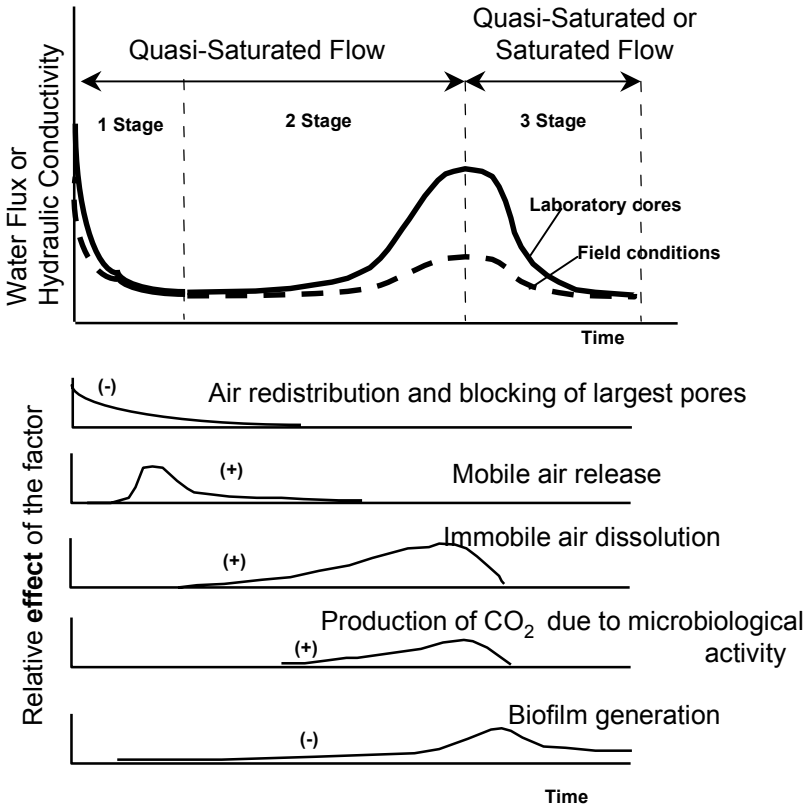
Quasi-Saturated Flow
Quasi-Saturated or
Saturated Flow
1 Stage
2 Stage
3 Stage
Water Flux or
Hydraulic Conductivity
Laboratory cores
Field conditions
Time
Relative effect of the factor
(-)
Air redistribution and blocking of largest pores
(+)
Mobile air release
Immobile air dissolution
(+)
Production of CO_2 due to microbiological
activity
(+)
Biofilm generation
(-)
Time

Figure 1

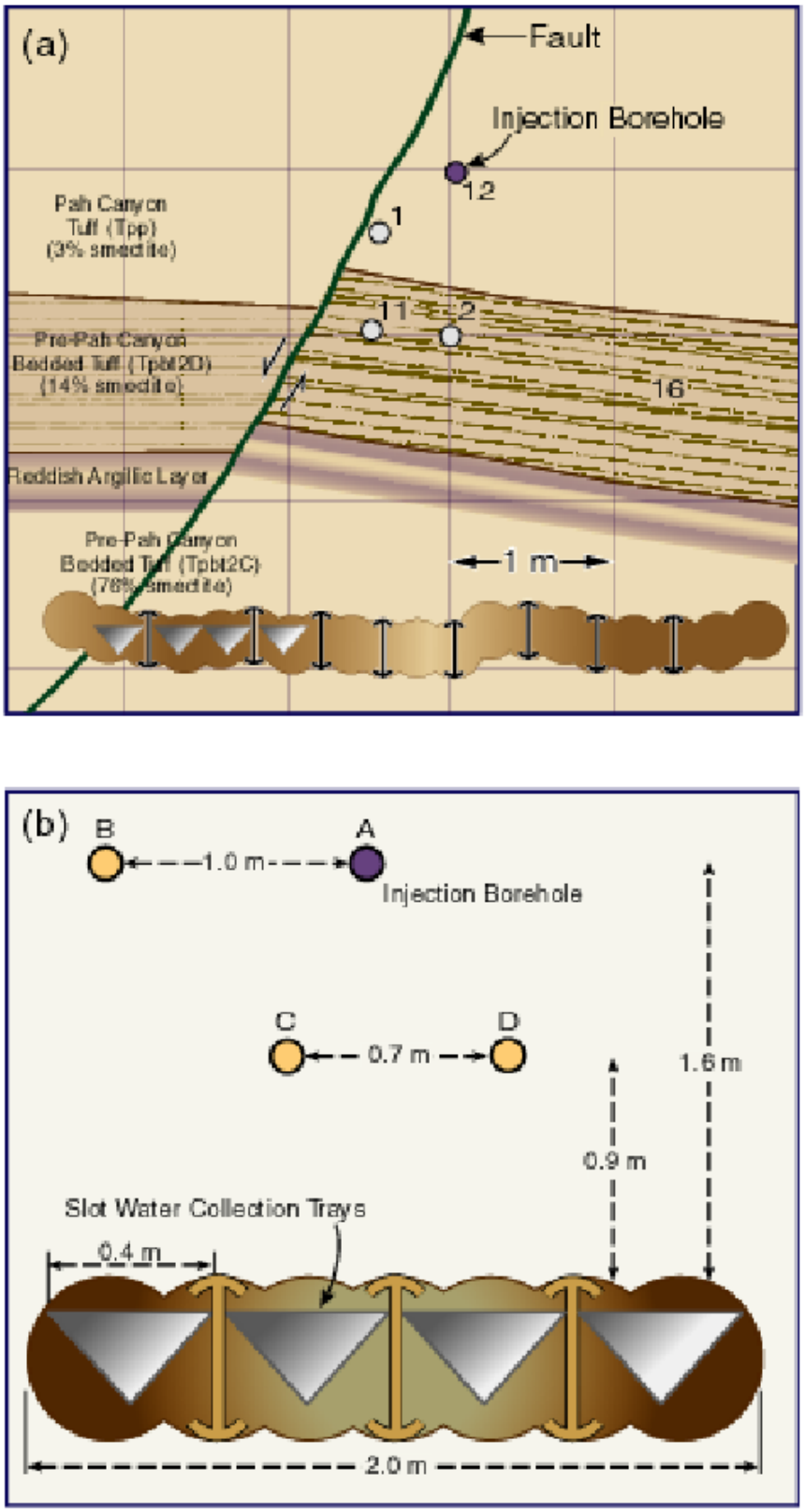
(a)
Fault
Injection Borehole
12
1
Pah Canyon
Tuff (Tpp)
(3% smectite)
11
2
Pre-Pah Canyon
Bedded Tuff (Tpbt2D)
(14% smectite)
16
Reddish Argillic Layer
Pre-Pah Canyon
Bedded Tuff (Tpbt2C)
(78% smectite)
1 m
(b)
B
A
1.0 m
Injection Borehole
C
D
0.7 m
1.6 m
0.9 m
Slot Water Collection Trays
0.4 m
2.0 m

Figure 2

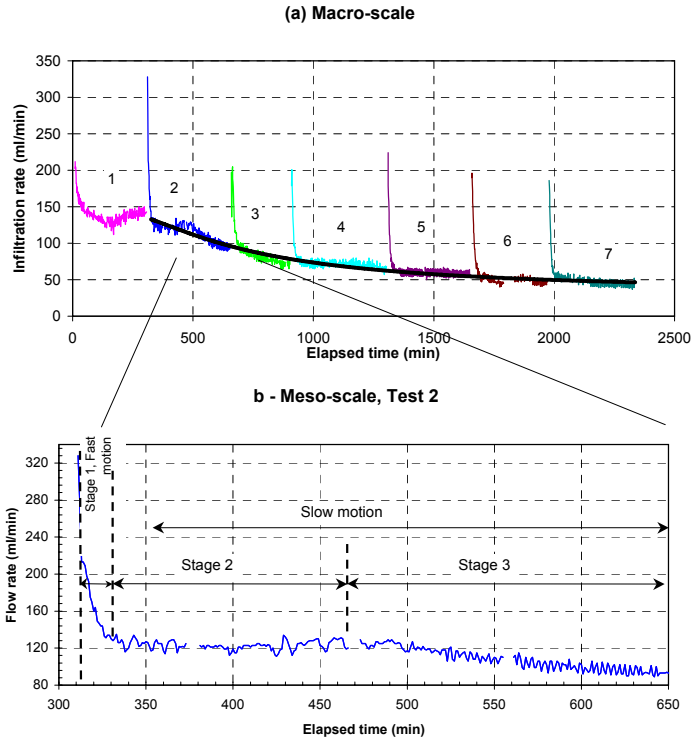
(a) Macro-scale
Infiltration rate (ml/min)
Elapsed time (min)
1
2
3
4
5
6
7
b - Meso-scale, Test 2
Flow rate (ml/min)
Stage 1, Fast motion
Slow motion
Stage 2
Stage 3
Elapsed time (min)

Figure 3

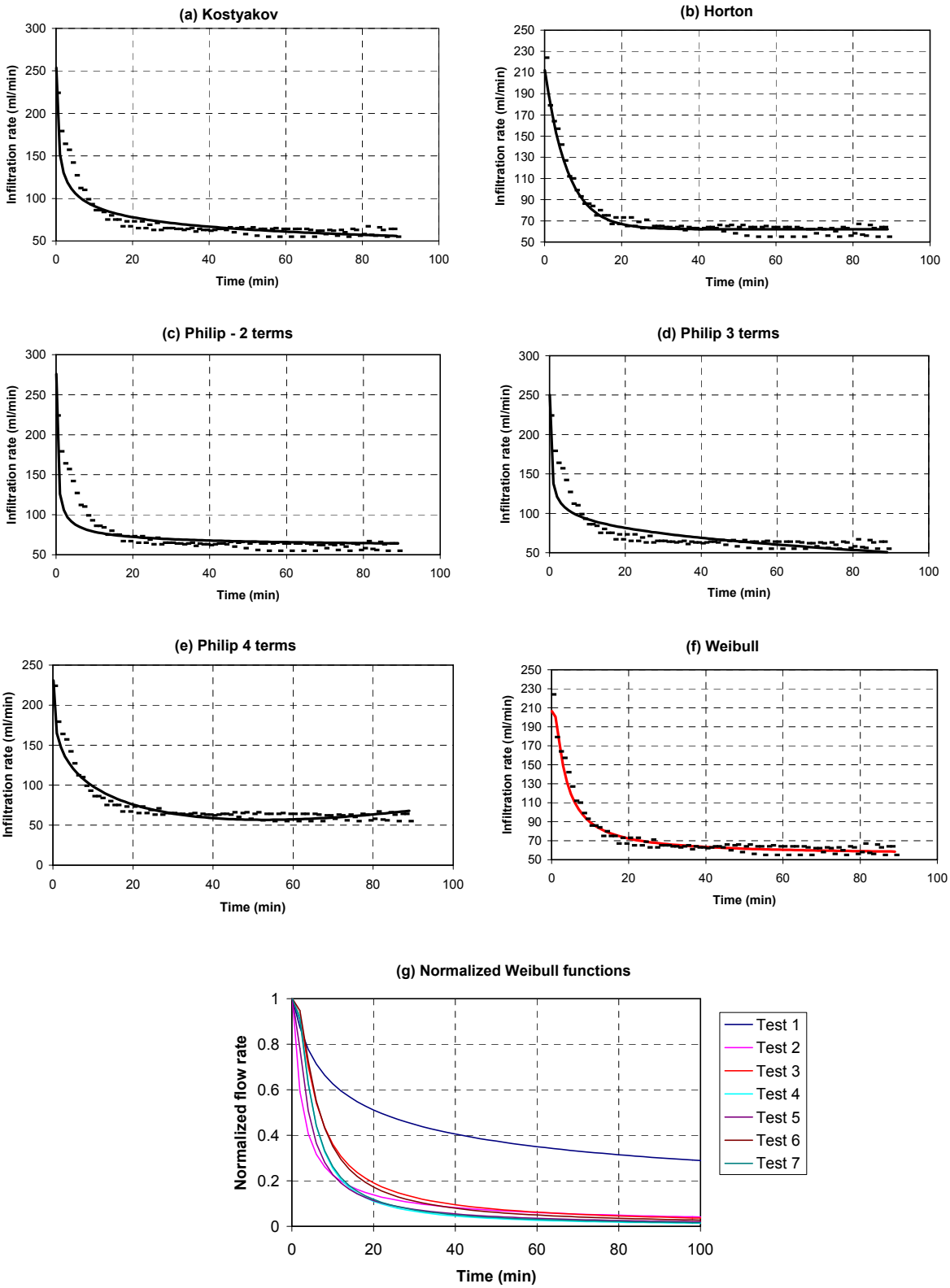
(a) Kostyakov
Infiltration rate (ml/min)
Time (min)
(b) Horton
Infiltration rate (ml/min)
Time (min)
(c) Philip - 2 terms
Infiltration rate (ml/min)
Time (min)
(d) Philip 3 terms
Infiltration rate (ml/min)
Time (min)
(e) Philip 4 terms
Infiltration rate (ml/min)
Time (min)
(f) Weibull
Infiltration rate (ml/min)
Time (min)
(g) Normalized Weibull functions
Normalized flow rate
Time (min)
Test 1
Test 2
Test 3
Test 4
Test 5
Test 6
Test 7

Figure 4

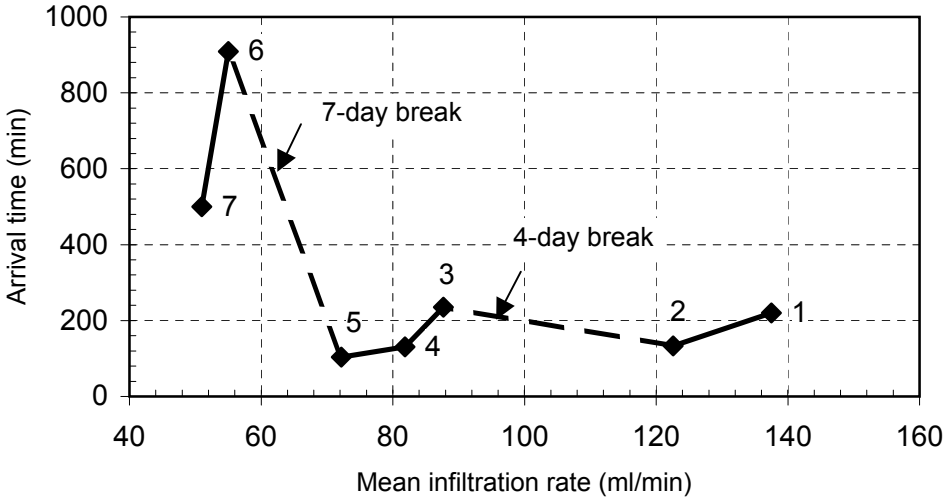
1000
800
600
400
200
0
Arrival time (min)
40
60
80
100
120
140
160
Mean infiltration rate (ml/min)
6
7-day break
7
4-day break
3
5
4
2
1

Figure 5

(a)

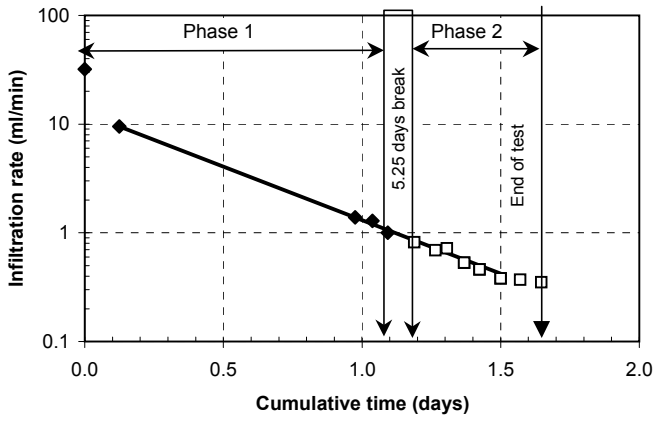
Phase 1
Phase 2
5.25 days break
End of test
Infiltration rate (ml/min)
Cumulative time (days)

(b)

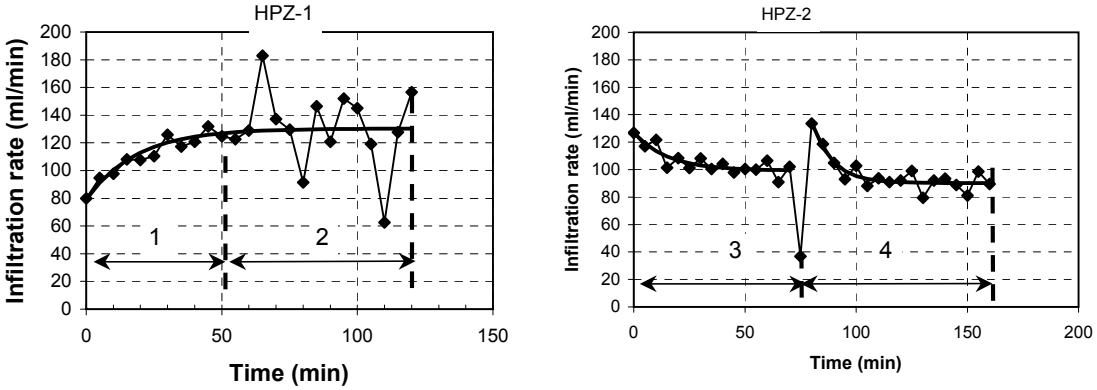
HPZ-1
HPZ-2
Infiltration rate (ml/min)
Time (min)
1
2
3
4

(c)

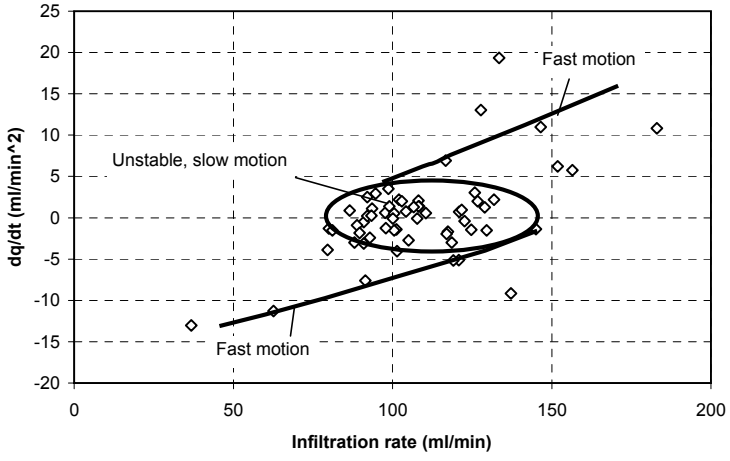
Fast motion
Unstable, slow motion
Fast motion
dq/dt (ml/min^2)
Infiltration rate (ml/min)

Figure 6

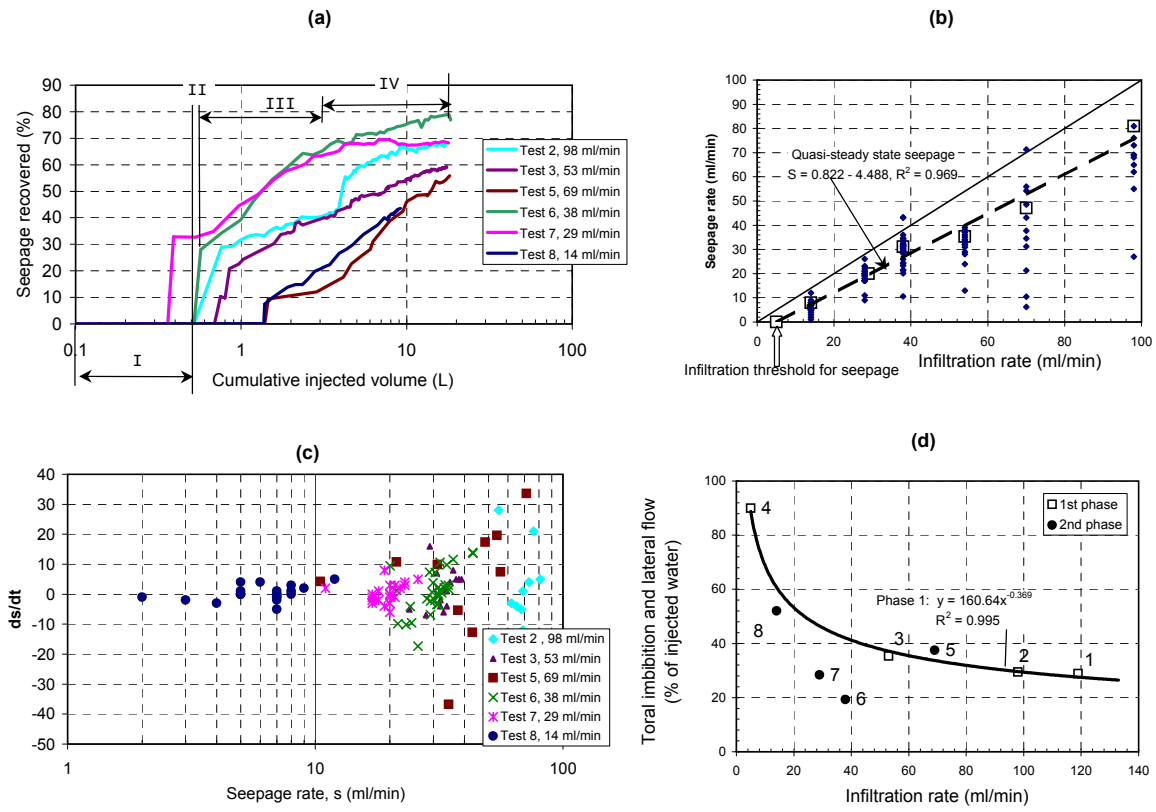
(a)
(b)
(c)
(d)
Seepage recovered (%)
Cumulative injected volume (L)
I
II
III
IV
Test 2, 98 ml/min
Test 3, 53 ml/min
Test 5, 69 ml/min
Test 6, 38 ml/min
Test 7, 29 ml/min
Test 8, 14 ml/min
Seepage rate (ml/min)
Infiltration rate (ml/min)
Quasi-steady state seepage
S = 0.822 - 4.488, R2 = 0.969
Infiltration threshold for seepage
ds/dt
Seepage rate, s (ml/min)
Toral imbibition and lateral flow
(% of injected water)
1st phase
2nd phase
Phase 1: y = 160.64x-0.369
R2 = 0.995

Figure 7

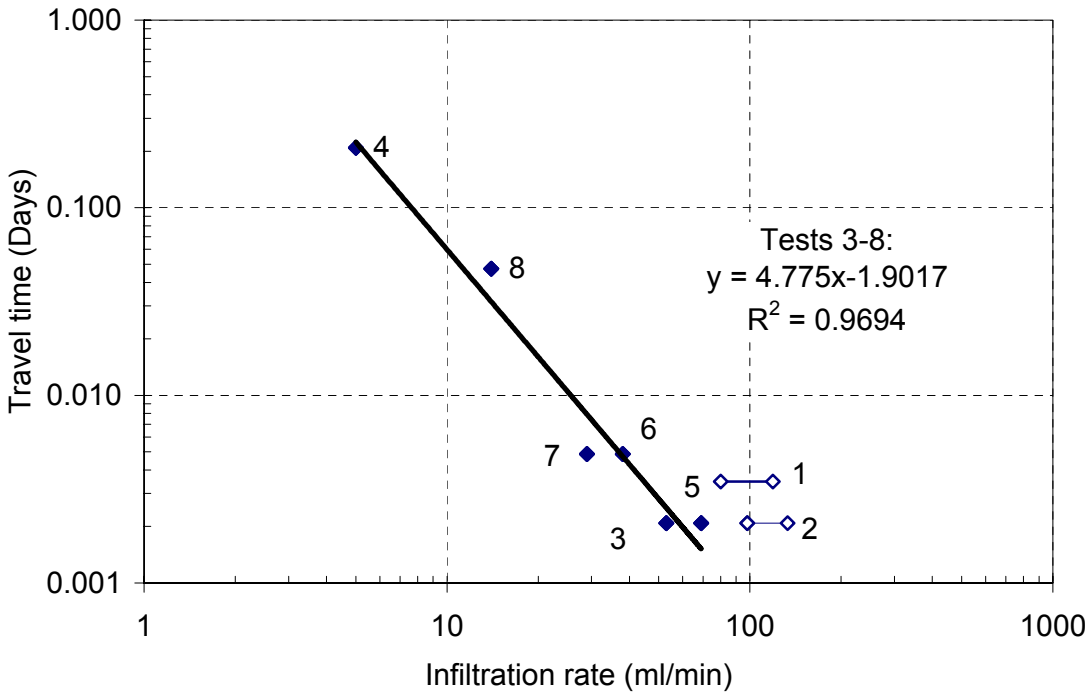
1.000
0.100
0.010
0.001
Travel time (Days)
1
10
100
1000
Infiltration rate (ml/min)
Tests 3-8:
y = 4.775x-1.9017
R2 = 0.9694
4
8
6
7
5
1
3
2

Figure 8

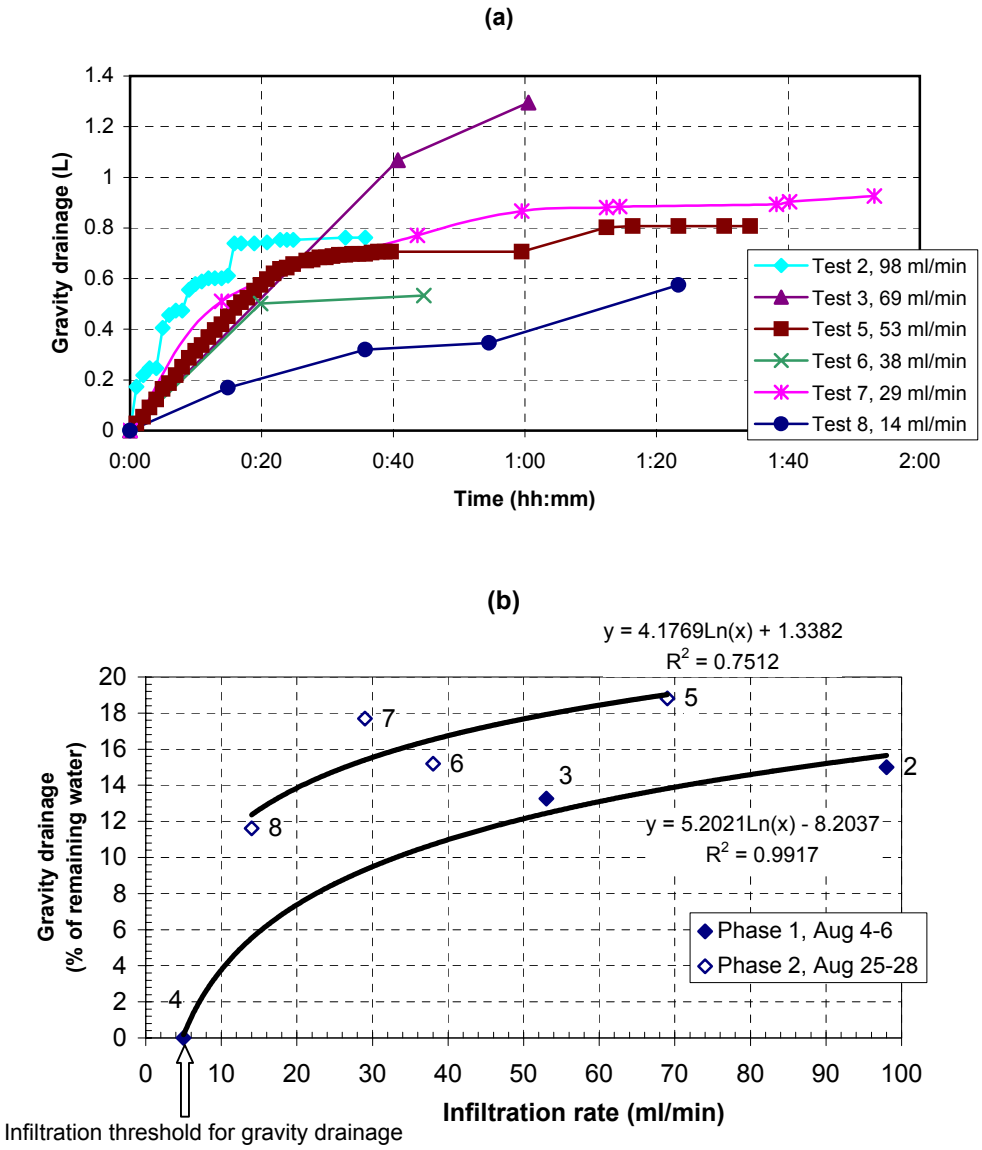
(a)
Gravity drainage (L)
1.4
1.2
1
0.8
0.6
0.4
0.2
0
0:00
0:20
0:40
1:00
1:20
1:40
2:00
Time (hh:mm)
Test 2, 98 ml/min
Test 3, 69 ml/min
Test 5, 53 ml/min
Test 6, 38 ml/min
Test 7, 29 ml/min
Test 8, 14 ml/min
(b)
y = 4.1769Ln(x) + 1.3382
R2 = 0.7512
y = 5.2021Ln(x) - 8.2037
R2 = 0.9917
Gravity drainage
(% of remaining water)
Infiltration rate (ml/min)
Phase 1, Aug 4-6
Phase 2, Aug 25-28
Infiltration threshold for gravity drainage

Figure 9

Table 1. Flow rates (ml/min) of infiltration tests carried out on August 4-6 (Phase 1) and August 25-28, 1998 (Phase 2) at Alcove 6.

	Phase 1				**Phase 2**			
Test number	1	2	3	4	5	6	7	8
Flow rate (ml/min)	**119***	**98***	53	5	69	38	29	14

*) The time-averaged flow rates are given for Tests 1 and 2 carried out under a constant head (7 cm). Other tests were carried out under a constant flow rate.

Table 2. Calculated parameters of Kostyakov, Horton, Philip, and Weibull equations for Test 3 at Alcove 4.

	Weibull	**Horton**	**Philip 2 terms**	**Philip 3 terms**	**Philip 4 terms**	**Kostyakov**
q_{max} (ml/min)	196.420	203.671				202.242
q_{min} (ml/min)	80.485	88.561	88.563	138.437	213.49	
s (min^{-1})	5.444					
d (dimensionless)	-1.084					
Horton β (min^{-1})		0.113				
S (Philip's sorptivity) (ml/ $t^{-0.5}$)			107.941	56.055	3.730	
B (Philip's equation) (ml/$t^{0.5}$)				-4.835	-22.870	
C (Philip's equation) (ml/t)					1.147	
n (Kostyakov exponent)						0.8420
Stnd Error	4.136	4.519	16.8407	10.652	5.801	9.490
Correlation Coefficient	0.987	0.984	0.752	0.910	0.974	0.928

Note: Philip's coefficient A is equivalent to q_{min} and is given in a row q_{min}.

Table 3. Parameters of Weibull's model for Alcove 4 infiltration tests, which were calculated assuming that the initial maximum value of the flow rate was at the time $t = 0.1$ minutes for each test

Tests	**1**	**2**	**3**	**4**	**5**	**6**	**7**
q_{max} (ml/min)	213.132	326.426	196.420	194.880	206.418	185.466	181.681
q_{min}(ml/min)	100.630	105.454	80.485	69.141	55.128	43.602	51.590
s (min^{-1})	2.849	1.543	5.444	6.310	3.247	6.757	5.747
d (dimensionless)	-0.461	-0.782	-1.084	-1.332	-1.100	-1.193	-1.275
ratio q_{max}/q_{min}	2.118	3.095	2.440	2.819	3.744	4.254	3.522
Estimated permeability, k (m^2)							
Fault	1.03E-11	1.57E-11	9.45E-12	9.37E-12	9.93E-12	8.92E-12	8.74E-12
Fault + matrix (volume averaged)	4.84E-12	5.07E-12	3.87E-12	3.33E-12	2.65E-12	2.1E-12	2.48E-12

Note: k was tentatively estimated from Darcy's law assuming a hydraulic gradient of unity and the flow area equal to the lower portion of the cylindrical opening of the borehole with 7.5 cm in diameter and 30 cm length. Permeability of 1.18 m^2 is equivalent to hydraulic conductivity of 1 m/day.

Table 4. Comparison of parameters of infiltration equations for the macro-trend of the infiltration rate for Tests 2 through 7 (only slow motion parts of each test are taken into account).

	Weibull	**Horton**	**Philip 2 terms**	**Philip 3 terms**	**Philip 4 terms**	**Kostyakov**
q_{max} (ml/min)	143.685	195.098				9023.379
q_{min} (ml/min)	32.014	43.592	-11.485	-12.192	80.434	
s (min^{-1})	9298.946					
d (dimensionless)	-1.434					
Horton β □(min^{-1})		0.0016				
S (Philip's sorptivity) (ml/ $t^{-0.5}$)			5423.305	5444.358	3615.211	
B (Philip's equation) (ml/$t^{0.5}$)				0.007318	-1.977	
C (Philip's equation) (ml/t)					0.0152	
n (Kostyakov exponent)						0.427
Stand Error	5.093	5.240	5.252	5.254	5.243	5.231
Correlation Coefficient	0.977	0.975	0.975	0.975214	0.975	0.975

Table 5. Fitting parameters of Horton formula and estimated permeabilities of Alcove 6 infiltration tests in a low-permeability zone

Test	**LPZ1**	**HPZ-1**	**HPZ-2**	
		Periods[*)]		
		2	**3**	**4**
q min	0.01**	79.17	**99.34**	**90.22**
q max	12.64	**130.32**	126.79	134.30
β	2.28	0.054	0.066	0.107
Estimated permeability (m^2)				
min	4.73E-16		4.70E-12	4.27E-12
max	5.98E-13	6.16E-12		

Notes: [*)] Periods are shown in Figure 6b; [**)] This value was fixed in the calculation.